

MAGNETIC GRAIN TRAPPING AND THE HOT EXCESSES AROUND EARLY-TYPE STARS

G. H. RIEKE, ANDRÁS GÁSPÁR, AND N. P. BALLERING
Steward Observatory, University of Arizona, Tucson, AZ, 85721
grieke@as.arizona.edu, agaspar@as.arizona.edu, ballerin@email.arizona.edu
Draft version October 3, 2018

ABSTRACT

A significant fraction of main sequence stars observed interferometrically in the near infrared have slightly extended components that have been attributed to very hot dust. To match the spectrum appears to require the presence of large numbers of very small (< 200 nm in radius) dust grains. However, particularly for the hotter stars, it has been unclear how such grains can be retained close to the star against radiation pressure force. We find that the expected weak stellar magnetic fields are sufficient to trap nm-sized dust grains in epicyclic orbits for a few weeks or longer, sufficient to account for the hot excess emission. Our models provide a natural explanation for the requirement that the hot excess dust grains be smaller than 200 nm. They also suggest that magnetic trapping is more effective for rapidly rotating stars, consistent with the average vsini measurements of stars with hot excesses being larger (at $\sim 2\sigma$) than those for stars without such excesses.

Subject headings: methods: numerical – circumstellar matter – infrared:planetary systems

1. INTRODUCTION

Planetary debris disks consist of dust and larger grains produced by planetesimal collisions, events that are driven through gravitational shepherding and stirring by planets (e.g., Liou & Zook 1999; Wyatt 2008). One might therefore expect the structure of debris disks to be so strongly affected by the placement of the planets and planetesimal belts that each system would be completely unique. However, it appears that there is a general regularity to debris disk structure (Su & Rieke 2014), with a very dilute terrestrial planet zone often marked by silicate emission, a denser zone roughly corresponding to our asteroid belt and lying near the snow line, an outer zone analogous to the Kuiper Belt, and a dilute halo consisting of small grains on highly elliptical orbits analogous to β meteoroids and in many cases also grains being ejected from the system by radiation pressure force. In addition, a fifth zone of hot emission predominantly around A-type stars (although found around some stars of later type) has been revealed by near-infrared interferometry near $2 \mu\text{m}$ (Absil et al. 2013; Ertel et al. 2014).

The hot component was an unexpected discovery, and a number of possible explanations were explored to explain it (e.g., Absil et al. 2008; Akeson et al. 2009), including (1) close companions; (2) stellar oblateness; (3) scattering of stellar emission by dust; (4) emission by optically thin gas; and (5) thermal emission by very hot dust. Although the first four may apply in a minority of cases, only the fifth appears capable of accounting for the hot emission in the majority of the stars where it is detected. van Lieshout et al. (2014) analyzed the ability of dust produced in conventional debris disk models to explain the hot emission. In these models, larger bodies are continuously ground down into smaller ones and dust by a cascade of collisions. The orbits of the small particles experience a number of forces. Stellar radiation provides a radial outward force and also an orbital-velocity-vector-dependent force, also known as Poynting-Robertson drag (PRD), which results in a slow inward circularized spi-

raling of a particle¹. The inward spiral gradually brings dust close to the star where it can become very hot; however, once the products of the collisions become small enough (sizes of order 3 - 7 μm around A-stars), they are ejected by radiation pressure force. Based on extensive analytic and numerical modeling of a specific case in which PRD brought grains inward from an outer ring, van Lieshout et al. (2014) showed that this conventional approach is unable to produce the spectral energy distributions (SEDs) and brightnesses at $2 \mu\text{m}$ characteristic of the hot excesses.

Generically, given the detections and detection limits at 2 and 10 μm (Absil et al. 2013; Mennesson et al. 2014; Ertel et al. 2014), producing the hot excesses requires a large population of sub-micron-sized dust particles, which under conventional debris disk models are quickly expelled from the vicinity of A-stars by radiation pressure force (e.g., Defrère et al. 2011; Lebreton et al. 2013). To date, the problem of retaining these small grains has not been solved (e.g., Bonsor et al. 2013), leading to models for enhanced inward planetesimal transport that are both very specific and quite complex (Raymond & Bonsor 2014; Bonsor et al. 2014) and thus difficult to picture around *all* the stars with hot emission.

This paper examines a number of aspects of the hot excesses, which in accordance with previous work we will assume arise through thermal radiation by small dust grains. We focus on hot excesses around A-stars, since this situation is most challenging to explain (given the strong radiation pressure force on small dust grains). We will address later-type stars briefly after the analysis of A-star excesses. In Section 2 we analyze near-infrared photometry to help confirm the reality of the hot excess emission independently of interferometry. We then explore the parameters required for hot dust to create this emission in Section 3. In Section 4, we show that the

¹ Stellar winds can produce forces analogous to those from stellar radiation, imposed by protons originating from the central star.

dust can be trapped by the stellar magnetic field to increase its dwell time near the star and thus to enhance its emission. Section 5 considers the effect of stellar type, magnetic field strength, and rotation on this behavior. Section 6 discusses the mass transport and equilibrium density of nanograins to compare with the requirements to create the hot emission. Section 7 describes how infalling comets and asteroids can enhance the mass transport where that is required to match the intensity of the hot excess. Section 8 tests some predictions of our model, and Section 9 summarises our results. Appendix A provides details of the photometry used in Section 2.

2. A TEST FOR THE PRESENCE OF HOT DUST DEBRIS

Slightly extended emission has been detected around many stars through interferometry at $2\ \mu\text{m}$ (see summary in Absil et al. (2013)), and around some at $1.6\ \mu\text{m}$ (Ertel et al. 2014) and at $10\ \mu\text{m}$ (Mennesson et al. 2014), through the reduced visibility compared with point reference sources. Given that these measurements are nearly all close to the limiting capability of the instruments, we report here an effort to confirm this effect using photometry. We will focus on the $J - K_S$ colors of stars of spectral types F6V and earlier. This range of spectral type is selected because later types have extreme sensitivity in this color to small errors in spectral type and/or stellar temperature, as well as to spectral absorption lines. This sensitivity makes the uncertainties in the $J - K_S$ color resulting from errors in stellar temperature too large for our purposes.

To begin, we determined the trend of $J - K_S$ color with stellar temperature. This color was selected to minimize systematic errors between different photometric systems (JHK usually being measured in a single system) and because the sublimation temperature of carbon grains suggests that the contrast of the hot dust emission relative to the star should be \sim five times lower at J than at K_S . We obtained 2MASS and visible (Pickles & Depagne 2010) photometry for the Hipparcos stars listed by McDonald et al. (2012). To have a uniform set of temperature estimates, we used the photometric approach of Casagrande et al. (2010). We utilized the relation for temperature on the basis of $V - K_S$ rather than those at shorter wavelengths because the long wavelength baseline and use of infrared bands should make the results less affected by interstellar reddening. We then fitted a 4th order polynomial to the trend of $J - K_S$ with temperature, and clipped outliers from successive fits down to the level of ± 0.15 mag. The survivors, 97.4% of the original sample, provided the final fit (Figure 1).

We next obtained J and K_S photometry for as many stars as possible from the near-infrared interferometric programs (Absil et al. 2013; Ertel et al. 2014), requiring spectral types of F6 or earlier and a consensus in the spectral type measurements (Skiff 2014) that the star is not a giant. Many of the stars are too bright for accurate modern photometry (e.g., in 2MASS) so we transformed heritage photometry into the 2MASS system as described in Appendix A. We compared the observed (and transformed) $J - K_S$ colors of all the stars within our spectral type criterion and with high quality photometry with expectations from the fit of the run of this color vs. temperature.

There were 41 stars altogether from Absil et al. (2013)

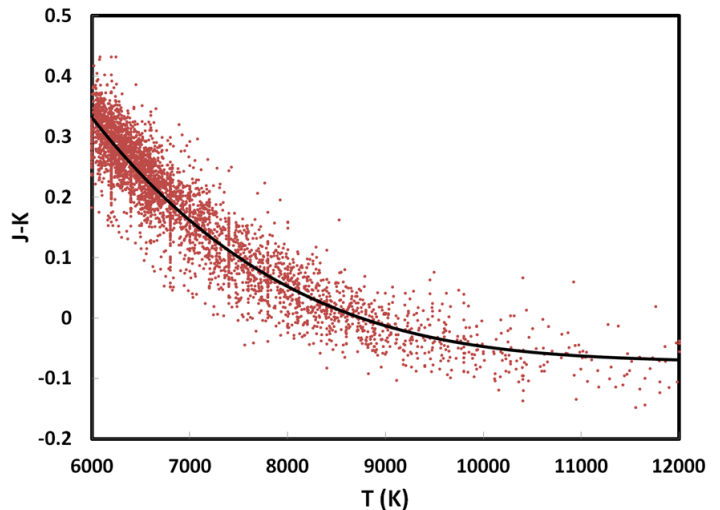


Figure 1. $J-K$ color vs. stellar temperature and the fourth-order fit used to represent the trend.

and Ertel et al. (2014) that met all of our requirements. The rms scatter for these stars around the expected $J - K_S$ was 0.017 mag. We found that the stars with identified hot excesses² have larger $J - K_S$ than the rest of the sample³ by 0.009 ± 0.006 mag (error of the mean). However, if the small additional red color is real, the temperatures of these stars from $V - K_S$ will be made to appear slightly cooler than they should be intrinsically. To estimate this effect, we corrected $V - K_S$ for every star with an identified excess downward by 0.01 mag and repeated the comparison, finding a corrected difference in $J - K_S$ of 0.011 ± 0.007 . The redder color relative to the fit of color vs. temperature is significant at about $1.5\ \sigma$, or equivalently there is only about a 6% probability of such a color being obtained by chance. Vega was not included in our calculations. It is discussed by Rieke et al. (2008), where it is shown that the contribution from the hot excess is of significant help in reconciling the observed colors with expectations; the photometry of this star alone supports the reality of the hot excess at the $\sim 1\ \sigma$ level.

To check against possible systematic errors due to the temperature estimates for the stars, we repeated this study using the temperatures from fits to the stellar SEDs in McDonald et al. (2012). The outcome was essentially identical - a redder $J - K_S$ by $\sim 1.5\ \sigma$ for the stars with reported hot excesses, compared to those without.

Although our result is not sufficiently strong to constitute a completely independent confirmation of the existence of the hot excesses, it supports their reality.

² HIP 27321, 57632, 58803, 60965, 91262, 92043, 93747, 97640, 105199, and 109422. HIP 109857 was eliminated because its excess is from a faint companion (Mawet et al. 2011) and HIP 28103 was not included because it is an X-ray source (Voges et al. 1999), indicating it also probably has a faint red companion star (De Rosa et al. 2011).

³ HIP 2802, 11001, 11783, 16245, 21589, 22499, 27288, 32362, 41307, 50191, 53910, 54872, 59774, 61622, 67275, 71284, 71908, 78702, 73996, 74824, 76829, 86486, 87108, 88175, 88771, 94114, 98495, 102333, 102485, 109285, and 111449

3. HOT DUST EMISSION PROPERTIES AND CONSTRAINTS

In the following section, we develop general constraints that a successful model for the K -band excesses must meet. As discussed in the Introduction, we assume that they arise as thermal emission from hot dust, rather than through scattering or by some other mechanism. We then compare these constraints in detail with previous work based on conventional collisional cascade debris disk models.

3.1. *Exploration of parameter space*

The primary observational constraint on models for the hot dust emission is the slope of the spectral energy distribution (SED) of the hot emission between 2 and 10 μm . The slopes are not identical for all stars - for example, the very blue slope indicated for Vega appears to differ significantly from the redder slope for η Crv⁴. However, three relatively well-measured systems, Vega, β Leo, and 10 Tau, have excess slopes as blue as, or bluer than, the photospheric SEDs of their (relatively hot) stars. Since these cases will be the most challenging for models, we adopt the constraint that the emitting dust should have a SED roughly Rayleigh-Jeans in behavior.

We used the Debris Disk Simulator (DDS) (Wolf 2015) to run an array of simple and relatively unconstrained models to understand the permissible ranges of key parameters: 1.) dust sublimation temperature; 2.) dust composition; 3.) minimum grain size; 4.) grain size distribution; and 5.) structure of the system - whether the dust is in a ring or a broader disk. We considered three grain compositions: carbon, as the best known grain to survive in high temperatures, MgO, and FeO⁵, thermally robust compounds produced in the thermal breakdown of silicates or sulfides (Mann et al. 2007). All models were run for an early A-star, $T = 9000$ K and $L = 16 L_{\odot}$.

The most favorable model systems consisted of very small grains in a narrow ring around the star. For this geometry, we explored the effect of different assumed sublimation temperatures, assuming optical constants appropriate for carbon, nanograins between 5 and 6 nm in size, and in a ring extending from the sublimation radius to 1.5 times this radius. Sublimation temperatures of ~ 1300 K or higher were sufficient to yield nearly Rayleigh-Jeans behavior between 2 and 10 μm ⁶. The primary effect of increasing sublimation temperatures was to decrease the mass in grains for a given output flux, by a factor of five from 1400 K to 2000 K and by another factor of two from 2000 K to 2600 K. At a sublimation temperature of 2000 K, a mass of about 10^{15} kg in 5.5 nm grains was sufficient

⁴ It is possible that the hot dust emission varies with time, complicating determining spectral slopes. In addition, the 10 μm measurements may have varying amounts of exozodi emission not related to the hot dust component

⁵ We used the DDS default optical constants for carbon and FeO and obtained constants for MgO from Palik (1997). A variety of grain materials of the type $\text{Mg}_x\text{Fe}_{1-x}\text{O}$ have similar optical behavior to FeO.

⁶ For the rest of the paper, we adopt sublimation temperatures of 2000, 1800, and 1900 K respectively for C, FeO, and MgO (e.g., Lamoreaux et al. 1987; Fedkin et al. 2006; Kazenas & Tsevtkov 2008). As a check, we verified that these values gave sublimation distances consistent with those in Mann et al. (2006)

to yield a hot excess of about 1% of the photospheric emission of an early A-star at 2 μm . Moreover, for small grains (< 200 nm) we found that the SEDs are similar for C and FeO, dominated by the drop in emission efficiency at wavelengths significantly longer than the grain size⁷. Pure MgO does not emit significantly at either 2 or 10 μm . We therefore concluded that these candidate materials in any combination (except pure MgO) could be responsible for the emission.

We next considered grain sizes and debris system geometries. In all cases we distributed the grains from the sublimation distance to an outer radius where there was a sharp cutoff in the grain density, and used the default density slope in the DDS of -1.5 . We found that a system with a single grain size needed to have that size less than 200 nm to yield the Rayleigh-Jeans SED; similarly, power law (index -3.5) size distributions from 0.01 μm to 10 μm or larger values were not consistent with this SED. We also found that grains in a narrow ring worked much better than distributing them into a disk with an outer radius even as small as 1 AU.

3.2. *Results from modeling specific hot excess systems*

Recent publications describing specific models of hot debris systems confirm the conclusions from this general exploration of parameter space (e.g., Absil et al. 2006; Akeson et al. 2009; Defrère et al. 2011; Lebreton et al. 2013; van Lieshout et al. 2014). Absil et al. (2006) and Defrère et al. (2011) showed that grain populations strongly emphasizing small sizes (a size distribution slope of -5 down to minimum grain sizes of 0.01 - 0.2 μm) at distances of predominantly 0.2 - 0.3 AU were needed to account for the hot excess around Vega. Akeson et al. (2009) found that the most natural fits to their measurements of hot dust emission around β Leo and ζ Lep required small (0.1 μm) refractory grains in narrow rings around the stars. Lebreton et al. (2013) found that the hot excess around Fomalhaut was best explained as due to a population of very small (size distribution slope of -6 from 0.01 to 0.5 μm) grains presumably mostly of carbon, and originating in a narrow ring near 0.09 - 0.24 AU. In all of these models, it was difficult to retain the very small grains close to the star in the face of radiation pressure force.

van Lieshout et al. (2014) tested whether the issue of grain blow out could be solved with a detailed model of grain inflow. They considered both analytic and numerical analyses, with inclusion of the tendency of the grains to pile up to high density at the sublimation radius as the grains are reduced in size and their β_{rad} (= photon pressure force/gravitational force) values increase, reducing the effective gravity they feel (Burns et al. 1979; Kobayashi et al. 2009). Their models had a parent body belt at a radius of 30 AU and with a particle size distribution of $n(s) \propto s^{-3.5}$ (where s is the particle radius) undergoing a collisional cascade, and then followed (in the numerical case) the flow of the products inward to the sublimation radius, where the size distribution was distorted by wave patterns to favor grains just above the blow out size. The calculations, carried out in great detail, encountered two fundamental problems: 1.) the SEDs produced were far too red to match

⁷ In this paper we quantify grain size in terms of radii.

the Rayleigh-Jeans slope shown by some of the hot-dust sources; and 2.) even with inclusion of the grain pileup at the sublimation radius, the emission was more than an order of magnitude too faint to account for the observed excesses at $2 \mu\text{m}$.

4. HOT EXCESSES FROM MAGNETICALLY TRAPPED NANOGRAINS

The above discussion illustrates the difficulties in accounting for the $2 \mu\text{m}$ excess emission with conventional debris disk theory. An alternative possibility is suggested by the demonstration by Mann et al. (2006) that nanograins in the inner Solar System could acquire an electrical charge and be trapped by the solar magnetic field through Lorentz force. In this section we show how a similar process could lead to the hot debris systems.

Many of the hot excesses are around A-type stars, which are often thought not to have magnetic fields and hence should not generate Lorentz forces. However, the discovery of weak fields around Vega (Lignières et al. 2009) and Sirius (Petit et al. 2011) showed this picture to be oversimplified. These fields are described by a “failed fossil” hypothesis in which the field left from the formation of the star is still evolving towards equilibrium. Under this hypothesis, A and B stars in general would have magnetic fields, but with values dependent on the stellar age, rotation rate, and initial field (Braithwaite & Cantiello 2013).

4.1. Grain charging

Small grains near hot stars will quickly acquire electrical charge either through the photoelectric effect, or by thermionic emission (Lefevre 1975). They will therefore inevitably interact with the stellar magnetic field, if there is one. The process of photoelectric grain charging has been modeled in detail by Pedersen & Gómez de Castro (2011); although their paper is focused on the effect around young stellar objects, the calculations for a 10,000 K blackbody are directly applicable to the situation for hot grains around main sequence A-stars. Although they assume grain properties for silicates, their results should be qualitatively applicable to the other grain materials under consideration for the hot emission, since the work functions for these materials are generally similar or smaller than those of silicates (see Weingartner & Draine (2001) for detailed comparisons of the behavior of silicates and carbonaceous material). Their numerical model accounts for the capture cross section for the incoming photon according to Mie theory, bases the electron yield on the prescription of Weingartner & Draine (2001), and includes the possibility that the resulting electric field from the positive charge of the grain is sufficient to cause it to recapture electrons that have escaped through the photoelectric effect. They find (their Figure 3) that a 30 nm grain in the radiation field of a 10,000 K blackbody very quickly (less than a second) acquires a charge of more than 100 electrons. For a hotter radiation field, their model shows a limiting charge of $q = s(\text{nm}) \times 27.5 e^-$ (where q is the total charge on a grain, s is the grain radius and e^- is the electronic charge), acquired in less than 0.1 second. Similar charge levels have been derived by Ma et al. (2013) and a similar size dependence has been found by Ignatov (2009). It is likely that similarly large charges will accumulate in

a 10,000 K radiation field within a few seconds.

4.2. Forces affecting the nanograins

We now construct a rough figure of merit to see when Lorentz force due to the stellar magnetic field is sufficiently strong to affect the dynamics of small grains. The dominant forces on small particles orbiting a hot star are gravitational, radiative, and electro-magnetic⁸. Particles can also be transported into the inner regions of circumstellar debris systems via PRD, another radiative effect, but it is a weak and slow-acting force. Because radiation pressure and gravitational forces are both proportional to r^{-2} , they are treated together and characterized through their ratio, β_{rad} (Burns et al. 1979). The combined force on a grain is then $1 - \beta_{\text{rad}}$ times equation (18) of Burns et al. (1979), i.e.,

$$F_{\text{grav+phot}} = (1 - \beta_{\text{rad}}) \frac{4 \pi s^3 \rho G M_*}{3 r^2} \quad (1)$$

where ρ is the density of the grain and s its radius, M_* is the mass of the star, and r is the distance of the grain from the star. The Lorentz force can be taken to be the vector product $\mathbf{v} \times \mathbf{B}$; we take the field strength B to have the radial dependence of a dipole ($\propto r^{-3}$). It can then be shown that the ratio of gravitational and photon forces on the grain to the Lorentz force is

$$\frac{F_{\text{grav+phot}}}{F_{\text{Lorentz}}} \approx 1.4 \frac{(1 - \beta_{\text{rad}}) \left(\frac{M_*}{M_\odot}\right)^{1/2} \left(\frac{s}{\text{nm}}\right)^2 \left(\frac{r}{\text{AU}}\right)^{3/2}}{k_q \left(\frac{v}{v_{\text{Kepler}}}\right) \left(\frac{B_*}{\text{Gauss}}\right) \left(\frac{R_*}{R_\odot}\right)^3}, \quad (2)$$

where k_q is the coefficient of the charge on the grain ($q = k_q \times s$) taken to have a density of $\rho = 2.7 \text{ g cm}^{-3}$, B_* is the magnetic field at the surface of the star, R_* is the stellar radius, v is the velocity of the field relative to the grain, and v_{Kepler} is the Keplerian velocity in the absence of any Lorentz forces. The magnetic field will rotate with the star out to a radius of $\sim 0.2 \text{ AU}$ (Section 4.3). For most A-stars, the local velocity of the rotating field will exceed the Keplerian velocity at all relevant radii.

For a grain near the blow out size around an early A-star, e.g., $s = 5000 \text{ nm}$, at a distance of 0.2 AU and with a surface magnetic field of 1 Gauss, Equation (2) shows that the Lorentz forces are completely negligible, by a factor $> 10^5$. However, Equation (2) shows the strong dependence on the grain size, and for a 10 nm grain at the same position (and with $k_q \sim 27.5$), Equation (2) indicates that the Lorentz force is dominant. Consequently, when a nanograin is launched into interplanetary space around the star, it will quickly become charged and then will be picked up by the magnetic field and will orbit the star with the field while performing Lorentz-force-confined epicycles around the field lines (Figure 2): the nanograin is trapped against being blown out by radiation pressure force.

4.3. Structure of stellar magnetic fields

⁸ Since winds are very small for typical early-type stars, their effects will be negligible.

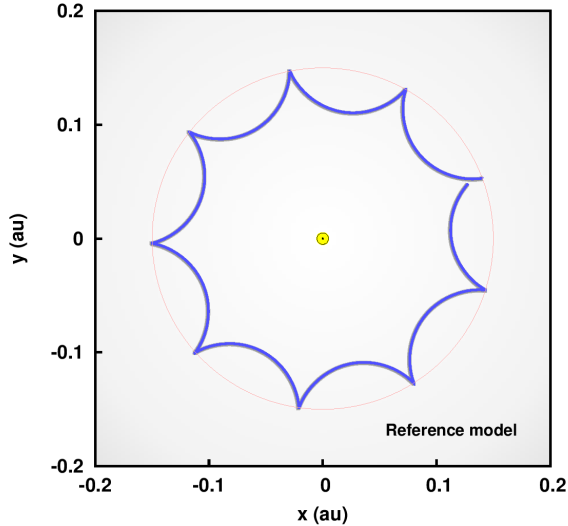


Figure 2. The first circumstellar orbit of the nanograin in the Reference model is shown in blue, following its production at the sublimation point. The thin red line shows the sublimation radius. The gyroradius is half the distance from this line to the innermost part of the epicycles. The point of view is looking down on the epicyclic orbit from a perspective above the pole of the star. The parameters of the reference model are summarized in Table 1.

The magnetic fields around A-stars must be reasonably well-organized or they would not be detectable in polarimetry of the full visible stellar disk. Although they may have somewhat more complex geometry (Alina et al. 2012), for simplicity we have assumed they are dipolar, i.e., fall off with distance, r , from the star $\propto r^{-3}$.

By analogy with the Solar System, we expect the magnetic field around early-type stars to have characteristic domains. Near the stellar photosphere, the magnetic field will be governed by the radial motion of the stellar plasma, whose density decreases rapidly outward. The second domain is where the magnetic field energy density is greater than the plasma energy density, therefore controlling the angular rotation of the field. The magnetic field will therefore be rotating with the central star in this domain. Further out, in the third domain, the magnetic field energy density decreases to values smaller than the stellar wind energy density, resulting in the formation of so called “Parker spirals” (Parker 1958; Schatten et al. 1969).

The nanograins in our models will either be in the second or third domain, as the first domain is very narrow and close to the photosphere. If they are in the third domain, we can assume the transverse velocity of the magnetic field to be equal to its value at the boundary between the second and third domains. The boundary of domains two and three can be found by equating the magnetic field and plasma kinetic energy densities,

$$\eta_{\text{magnetic}} = \frac{B(r)^2}{2\mu_0}, \quad (3)$$

$$U = \frac{1}{2}\rho(r)v_{\text{sw}}(r)^2, \quad (4)$$

with

$$B(r) = B_* \frac{R_*^3}{r^3}, \quad (5)$$

$$\rho(r) = \frac{\dot{M}}{4\pi r^2 v_{\text{sw}}(r)}, \quad (6)$$

where η_{magnetic} is the magnetic field energy density, U is the plasma kinetic energy density, $B(r)$ is the magnetic field strength at a distance r from the star, decreasing in strength as a dipole, $\rho(r)$ is the stellar wind matter density as a function of distance from the star, v_{sw} is the stellar wind speed as a function of distance from the star, and μ_0 is the vacuum permeability. The boundary between the regions can then be found at

$$r = \left[\frac{4\pi B_*^2 R_*^6}{\mu_0 \dot{M} v_{\text{sw}}(r)} \right]^{\frac{1}{4}}. \quad (7)$$

The exact behavior of the stellar wind or the mass loss rate of early-type stars is not known. Theoretical models (e.g., Babel 1995) predict mass loss rates around 2 orders of magnitude less than the solar one, at $\dot{M} \approx 10^{-16} M_{\odot} \text{ yr}^{-1}$. Using these values, we calculate the boundary between domains 2 and 3 to be at 0.19 AU from an early-type star (reference model introduced in Section 4.5), near the sublimation radius. In Section 4.4, we explore the effects of varying the stellar rotation rate, therefore effectively also exploring the effects of the boundary being located closer to the star.

4.4. Gyroradius and maximum trapped grain size

We now investigate the orbital stability of the nanograins produced near the sublimation radius. We focus on the particle size range that can be trapped in the rotating stellar magnetic field and the timescale to spiral inward to the central star. For simplicity, we assume the nanograins originate at the sublimation radius from large particles that are dragged inward from an external location. The sublimation temperature is taken to be between 1300 and 2300 K, which corresponds to a narrow distance range of 0.2 - 0.07 AU from an A0 spectral-type star. Initially, the nanograins adopt the orbital velocity of the parent particle. The primary loss mechanism is collisions, for which the probability depends on the nanograin volume density. To estimate the collision rate, we will also model the spatial distribution of particles.

We set a reference model roughly representative of most hot-excess systems, as summarized in Table 1. Since $\beta_{\text{rad}}(s)$ levels off to a constant for all nanograins smaller than around 20 nm (see Figure 3), we assume it to be independent of grain size for all the models in this section, although will use size dependent values for models in Section 5.

The motion of the magnetically trapped nanograins is described to first order by their epicycles with amplitudes equal to the gyroradius (Larmor radius or cyclotron radius), circling the star at a distance determined by the grain release point. The gyroradius of a particle defines the volume of space within which a particle of its size is confined; therefore it also determines the collisional timescale of the particle. Hence, it is important to understand the range of values it can take. The gyroradius can be found by equating the sum of the forces acting on

Table 1
Parameters of the Reference model.

Variable	Description	Fiducial value
M	stellar mass	$2.4 M_{\odot}$
B_*	magnetic field strength at stellar surface	1.0 Gauss
R_*	stellar radius	$2.3 R_{\odot}$
r_{sub}	sublimation radius	0.15 AU
s	nanograin radius	5 nm
ρ	nanograin density	2.7 g cm^{-3}
$\beta_{\text{rad;nano}}$	nanograin radiative coefficient	6.0
$\beta_{\text{rad;parent}}$	parent particle radiative coefficient	0.2
P_{rot}	rotation period of star	10 hours
Ω_{ast}	angular frequency of the central star	$2\pi P_{\text{rot}}^{-1}$
k_q	electric charge coefficient	$27.5 e^-/\text{nm}$

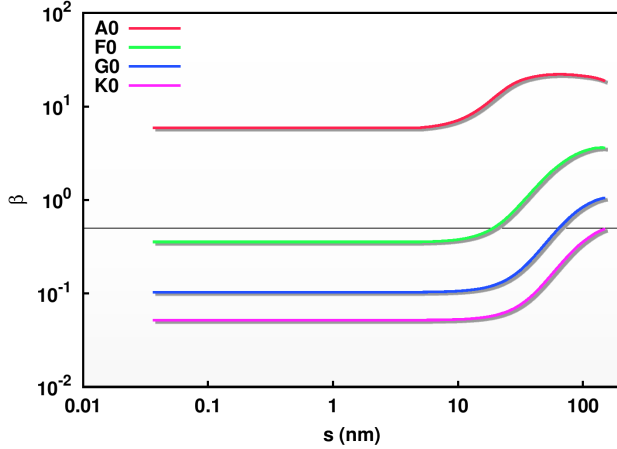


Figure 3. The values of $\beta_{\text{rad}}(s)$ used in section 5 for various spectral-type sources.

the nanograin (gravitational, electro-magnetic Lorentz, radiative blowout and centripetal forces) to zero. For an analytic estimate, we will assume that PRD is negligible compared to the other forces. Therefore we can write

$$\frac{\mu(\beta_{\text{rad;nano}} - 1)}{r_{\text{sub}}^2} + \frac{q}{m}(v_{\text{gyro}} + v_{\text{orb}} - \Omega_{\text{ast}}r_{\text{sub}})B_*\frac{R_*^3}{r_{\text{sub}}^3} + \frac{v_{\text{gyro}}^2}{r_{\text{gyro}}} + \frac{v_{\text{orb}}^2}{r_{\text{sub}}} = 0. \quad (8)$$

The variable μ is the standard gravitational parameter of the central star ($\mu = GM_*$), m is the particle mass, and Ω_{ast} is the angular frequency for the rotation of the central star. Here we determine the Lorentz and centripetal forces on the particle at its furthest location from the central star on its epicycle. The charge a nanograin accumulates is $q = k_q s$. The orbital and gyro-rotational velocity a nanograin acquires depend on its inertia. Small nanograins will accelerate close to the speed of the magnetic field, while the largest trapped grains will remain near the parent particle's velocity:

$$v_{\text{orb}}(s \ll s_{\text{max}}) \approx \Omega_{\text{ast}}r_{\text{sub}} \quad (9)$$

$$v_{\text{orb}}(s \sim s_{\text{max}}) \approx v_{\text{parent}}, \quad (10)$$

where s_{max} is the largest trapped particle, $\Omega_{\text{ast}} = 2\pi P_{\text{ast}}^{-1}$, and the orbital velocity of the parent particle is

$$v_{\text{parent}} = \sqrt{\frac{\mu(1 - \beta_{\text{rad;parent}})}{r_{\text{sub}}}}. \quad (11)$$

We approximate the gyrotational velocity of the small nanograins to be

$$v_{\text{gyro}}(s \ll s_{\text{max}}) \approx v_{\text{parent}} - \Omega_{\text{ast}}r_{\text{sub}}. \quad (12)$$

i.e., assuming that the particle retains its initial velocity relative to the magnetic field, $v_{\text{parent}} - \Omega r_{\text{sub}}$. The gyroradius of a small nanograin is then expressed by

$$r_{\text{gyro}} = \frac{r_{\text{sub}}^3 (v_{\text{parent}} - \Omega_{\text{ast}}r_{\text{sub}})^2}{r_{\text{sub}}\mu(1 - \beta_{\text{r;n}}) - \Omega^2 r_{\text{sub}}^4 - B_* R_*^3 (v_{\text{parent}} - \Omega r_{\text{sub}}) \frac{q}{m}}. \quad (13)$$

The gyroradius of our reference model particle is 0.066 AU. The largest nanograin that the field can trap will remain in a circular orbit around the star with the velocity of the parent particle, since for this case the Lorentz force just cancels the radiative force. The centripetal force and gyrotational velocity are not defined in this case. This yields a largest particle size of

$$s_{\text{max}}^2 = \frac{3k_q B_* R_*^3 (\Omega_{\text{ast}}r_{\text{sub}} - v_{\text{parent}})}{4\pi\rho\mu r_{\text{sub}} (\beta_{\text{rad;nano}} - \beta_{\text{rad;parent}})}. \quad (14)$$

Solving this equation for our reference model yields an upper limit of 121 nm on the size of the nanograins trapped by the magnetic field of the reference system. A narrow range of larger particles, that would otherwise be removed via radiative pressure blowout (if $\beta_{\text{rad;nano}} > 0.5$), remain in the system with “inverse” epicycles outside of the sublimation point. The lower limit on the distribution is set by the molecular limit (a grain must consist of a number of molecules) to be several tenths of a nm.

4.5. Numerical analysis of the orbital dynamics

We now augment and illustrate these arguments with a numerical model. The accelerations of a grain are:

$$\mathbf{a}_{\text{gr}} = -\mu \frac{\mathbf{r}}{r^3} \quad (15)$$

$$\mathbf{a}_{\text{rad blow}} = \mu\beta_{\text{rad}} \frac{\mathbf{r}}{r^3} \quad (16)$$

$$\mathbf{a}_{\text{rad drag}} = -\frac{\mu\beta_{\text{rad}}}{cr^2} \left(\dot{r} \frac{\mathbf{r}}{r} + \mathbf{v} \right) \quad (17)$$

$$\mathbf{a}_{\text{em}} = \frac{q}{m} (\mathbf{v} - \Omega_{\text{ast}} \times \mathbf{r}) \times \mathbf{B}. \quad (18)$$

The various accelerations are: gravitational (\mathbf{a}_{gr}), radiative blowout ($\mathbf{a}_{\text{rad blow}}$), radiative drag - PRD ($\mathbf{a}_{\text{rad drag}}$), and electromagnetic Lorentz (\mathbf{a}_{em}). c is the speed of light and \mathbf{v} is the relative motion of the particle w.r.t. the central star.

By necessity, the analytic analysis neglected several important physical effects, an issue we address here. The trapped particles will experience minor perturbations from PRD, varying electro-magnetic forces along their gyro-orbits (due to the strong radial dependence of the magnetic field), and also varying gravitational force along the gyro-orbits. Furthermore, the orbital and gyro-velocity of the largest trapped particles depend on the mass of the nanograins. We evaluate these effects with numerical methods, finding that they result in a slow orbital decay of the particles and also lead to smaller gyroradii for the larger nanograins still trapped by the magnetic field.

We initiate the numerical analysis by tracing the orbital evolution of a “large” ($\sim 10 \mu\text{m}$) parent particle subject to the accelerations in Equations (15 - 18), which is dragged in via PRD from an external location without undergoing collisions. The exact initial orbit of the parent particle is irrelevant, as its orbit will be circularized by the PRD by the time it approaches the point of sublimation. At that point, we replace the parent particle with a charged nanograin, and thereafter its orbit will be mostly determined by the radiative blowout force and the electro-magnetic Lorentz force from its interaction with the rotating stellar magnetic field. These forces place the trapped nanograin on an epicyclic orbit.

We will assume the particles have an orbital inclination of $i = 0$ and that the stellar magnetic field vector is perpendicular to the particle orbital plane. We set the stellar magnetic field to be coupled to the stellar rotation (as described in section 4.3). The dynamical evolution of the particles is evolved using an adaptive step-size 4th order Runge-Kutta integrator, with an allowed relative numerical error of 10^{-12} per step.

In Figure 2, we show the orbit of the 5 nm particle in our Reference model. The particle has a gyroradius of ~ 0.018 AU, with a gyro-period of 1.6 hours and an orbital period around the star of 0.59 days. Therefore, the particle has roughly 9 epicycles in a single orbit. The particle is orbiting in its epicycle at 340 km s^{-1} and at 2773 km s^{-1} around the star. The gyroradius given by the numerical solution is far from the value given by the analytic approximation, which yields 0.066 AU. As noted before, the offset is due to the approximation that the gyro-velocity will be equal to the difference between the orbital velocity of the parent particle and the projected velocity of the magnetic field.

In Figure 5, we show the orbital decay of the particle, assuming it to be undisturbed by collisions. The nanograin of our reference model would remain in the system for a few decades. Finally, we plot both the analytic estimate and the numerical solution of the gyroradius as a function of particle size in the reference system in Figure 4. The analytic approximation agrees with the numerical solution up to a few nm in size, from which point the analytic solution yields larger gyroradii. The largest particle size given by the analytic analysis (Equation 14) agrees with the result from the numerical model. The numerical analysis shows that particles larger than s_{max} are also placed on gyro-orbits outside of the sublimation point.

5. MODEL DEPENDENCE ON VARIABLES

In this section we investigate how the dynamical evolution of the nanograins depends on the system variables. We are mainly interested in the size-range and location of the trapped particles and their absolute velocities within the system to allow estimates of collisional timescales. We consider the effects of (1) the spectral-type of the central star; (2) the magnetic field strength; and (3) the rotation period of the central star. We do not investigate the dependence on the electric charge coefficient, k_q , as it is a multiplicative constant of the magnetic force, so varying it is equivalent to changing the magnetic field strength. Unlike in the previous section, we will assume $\beta_{\text{rad}}(s)$ to vary with particle size to provide a more realistic understanding of the nanograin dynamics in various

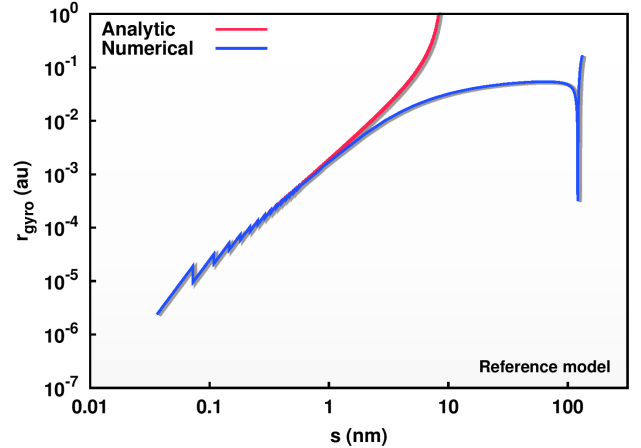


Figure 4. The analytic and numerical solutions of the gyroradius as a function of particle size in the reference model, assuming $\beta_{\text{rad;nano}}$ is independent of particle size. The “sawtooth” at the smallest sizes is due to the quantized nature of charge. The analytic estimate breaks down for larger sizes, where the inertia of the particles is too large for them to be accelerated to the angular rotation of the magnetic field. Furthermore, larger nanograins are also trapped in gyrotational orbits outside the sublimation point (see the break in the numerical analysis).

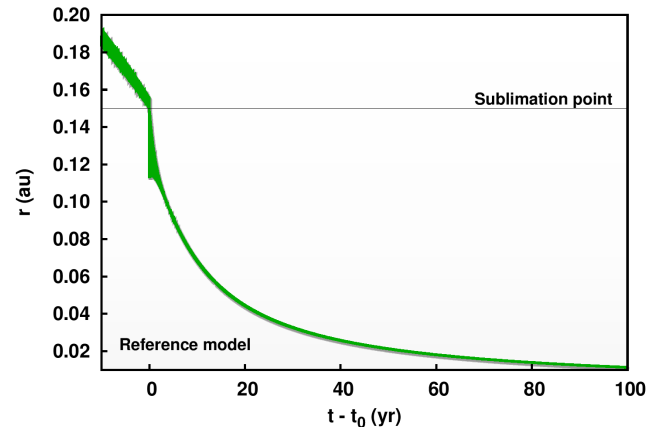


Figure 5. The orbital decay of the nanograin in the Reference model. The radial distance before sublimation varies due to the initial ellipticity ($e=0.01$) of the parent particle’s orbit.

systems. We plot the $\beta_{\text{rad}}(s)$ values we use in our models as a function of particle size and stellar spectral type in Figure 3.

5.1. Dependence on the spectral-type

We analyze the gyro-orbits of nanograins around A0, F0, G0, and K0 spectral-type stars in this subsection. The variables of the modeled systems are summarized in Table 2. As Figure 3 shows, the $\beta_{\text{rad}}(s)$ values of nanograins around most stars do not reach 0.5, i.e. the nanograins will not be blown out of the system by radiation pressure force. However, the interactions with stellar winds around the later type stars have a strong influence on the grains, creating a pseudo-PRD drawing grains inward and also carrying small grains out of the system. Grain charging by photoelectric effect is less effective for late-type stars, but charging can also oc-

Table 2

Variables of various spectral-type systems analyzed in section 5.1. The remaining variables are kept at the same values as in the reference model and the $\beta_{\text{rad;nano}}$ is a function of particle size, as described in the text. Due to the size dependent $\beta_{\text{rad;nano}}$, s_{max} will take a different value from the analytic prediction.

Spectral type	M_* (M_\odot)	R_* (R_\odot)	r_{sub} (AU)	s_{max} (nm)
A0 [Reference model with $\beta_{\text{rad}}(s)$]	2.40	2.30	0.15	62
F0	1.70	1.30	0.13	87
G0	1.10	1.05	0.06	141
K0	0.78	0.85	0.03	186

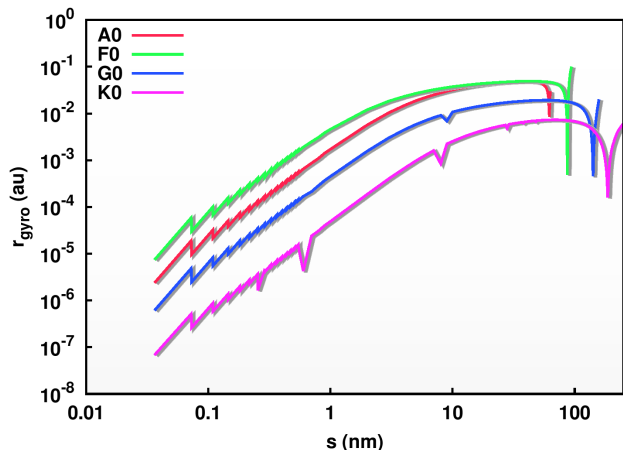


Figure 6. The gyroradius as a function of particle size around various spectral type stars; in this case, we have used values for β_{rad} illustrated in Figure 3.

cur through thermionic emission and electron impacts from the stellar wind plasma. Unless the grains are very hot, their charge is set by an equilibrium between the first (which drives their charge positive) and the second (which drives them negative). A detailed analysis for the Solar System is provided by Mann et al. (2014), where it is demonstrated that the resulting electrical charges can cause nanograins within ~ 0.15 AU of the Sun to become trapped in the solar magnetic field against being carried away by the solar wind. The behavior around other stars of roughly solar type should be similar.

Although the expected behavior is complex because of interactions with the stellar wind (Mann et al. 2014), it is illustrative to examine the simple version provided by our model. In Figure 6, we plot the gyroradii of the particles in these systems. The largest particles the systems are able to retain increase with later-type stars. Furthermore, the characteristic collisional velocities decrease for later-type stars, as shown in Figure 7. Therefore, the effects of magnetic field trapping could be more evident around them, as the collisional probabilities of the particles decrease with the collisional velocities. It is worth noting though, that the models presented here maintain the fast 10 hour rotation of the Reference model which may not be a common value for most later-type systems. Increasing the rotation period will decrease the effects of magnetic field trapping and thus the production of hot excess (see Section 5.3).

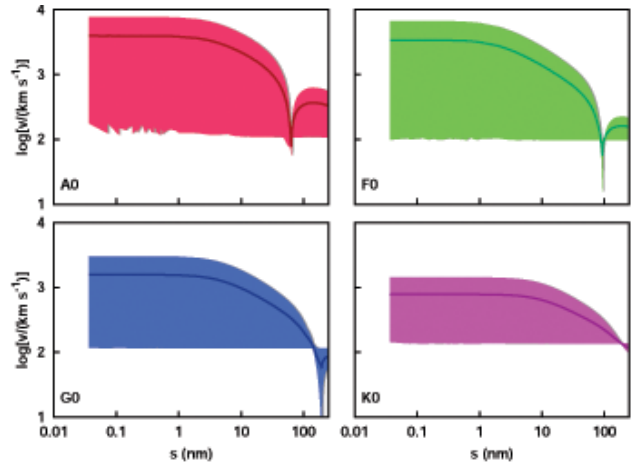


Figure 7. The absolute velocity range as a function of particle size around various spectral type stars. The shaded region shows the range of velocities, while the line is the orbit-averaged value.

5.2. Dependence on the magnetic field strength

In this subsection, we investigate the sensitivity of the trapping mechanism to varying magnetic field strengths. Peculiar Ap spectral-type stars are known to have over 100 G magnetic fields. Therefore, we model a three order of magnitude range of magnetic fields to study their effects, from 0.1 to 100 Gauss. In Figure 8, we show the gyroradii of the particles around the A0 star (reference) model, with size dependent $\beta_{\text{rad}}(s)$ values. The model allows large variations in the magnetic fields. A magnetic field even as weak as 0.1 Gauss⁹ is able to retain a relatively large range (s up to 23 nm) of particle sizes near the sublimation radius. The velocities of the particles do not depend on the strength of the magnetic field (Figure 9), therefore the collisions around systems with strong fields will not be more violent than in systems with weak fields. Systems with stronger fields will be able to keep larger particles within their systems. However, the gyro-radii of the particles will be orders of magnitude smaller, resulting in much larger collisional probabilities and more rapid loss of the grains. The relative number of large particles is likely to be small (the size distribution from nanoparticle production mechanisms is thought to favor tens of nm) and hence the emission from a system where only the few large particles survive is likely to be weak. Therefore, it is unlikely that large magnetic fields will lead systematically to strong hot excesses.

The magnetic fields in early-type stars are primordial, therefore we do not have to model the effects of periodic magnetic field flipping. However, systems where the rotational direction of the magnetic field and that of the nanograins are not aligned are plausible. In Figure 10, we plot the gyroradii of particles shown in Figure 8, but with the direction of the magnetic field flipped. The system is still able to maintain particles within the system, although further out from the sublimation radius on “inverse” epicycles and less effectively (over a smaller range of grain size).

⁹ and therefore smaller than the fields of 0.2 ± 0.1 G measured for Sirius (Petit et al. 2011) and 0.6 ± 0.2 G for Vega (Lignières et al. 2009)

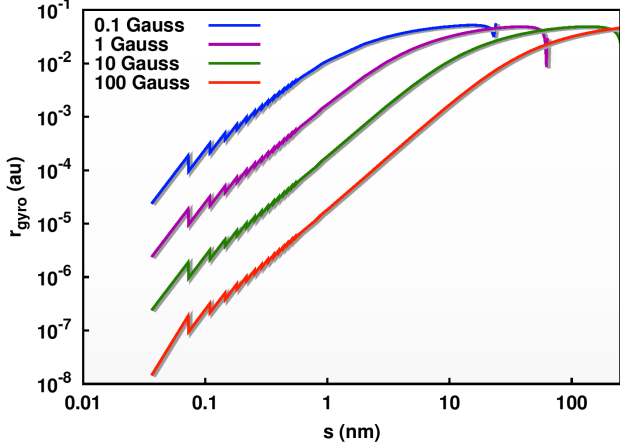


Figure 8. The gyroradius as a function of the magnetic field strength for various size particles in the reference model, with β_{rad} as in Figure 5.

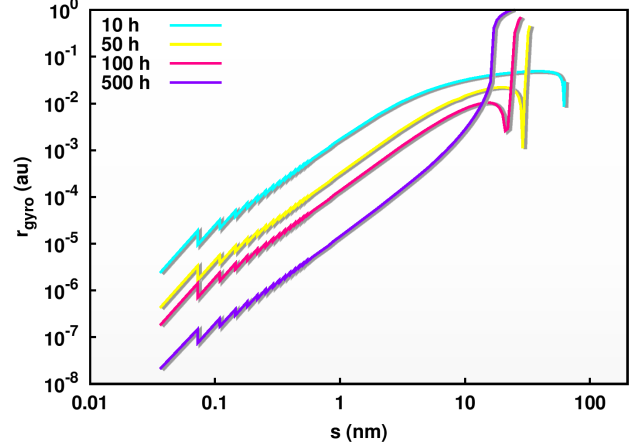


Figure 11. The gyroradius as a function of the stellar rotation period for various size particles in the reference model.

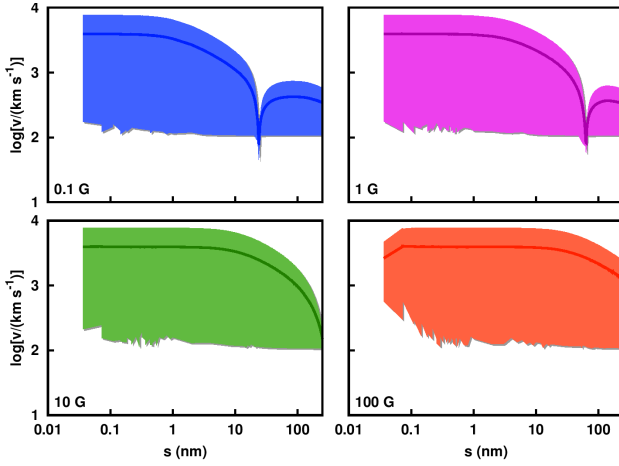


Figure 9. The absolute velocity range (shaded region) as a function of the magnetic field strength for various size particles in the reference model. The lines show the orbit-averaged values

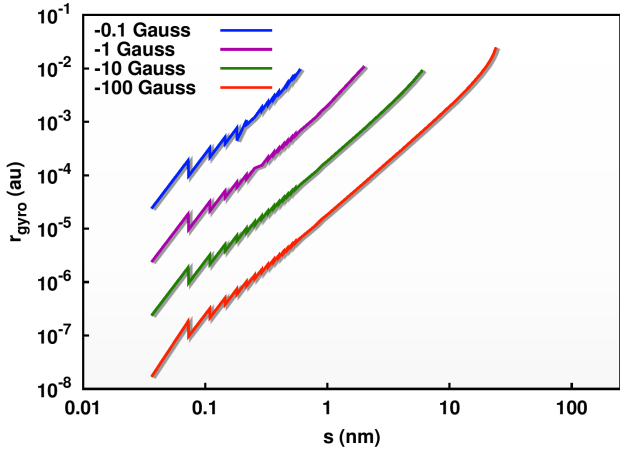


Figure 10. The gyroradius as a function of the magnetic field strength for various size particles in the reference model, with the direction of the magnetic field flipped.

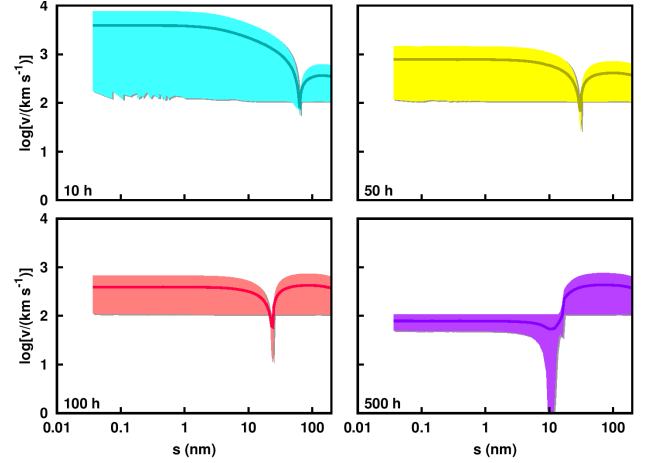


Figure 12. The absolute velocity range (shaded) as a function of the stellar rotation period for various size particles in the reference model. The lines are orbit-averaged values.

5.3. Dependence on the stellar rotation period

The faster a star rotates, the faster the magnetic field rotates with it and hence the stronger will be the electromagnetic forces. In Figure 11, we show the gyroradii of particles in the reference system, varying the rotation period of the central star. Within the typical rotation rate of early-type stars, nanograins of sizes up to 20-50 nm are expected to be trapped, with high velocities of motion, up to a few thousand km s^{-1} .

Figure 11 shows that more rapidly rotating stars are able to trap larger nanograins. In Sections 6.2 and 6.3 we show that these larger particles have smaller collisional cross sections and longer lifetimes; while their common orbital velocities will be large, they will interact at their gyroradial velocities, which will be smaller (due to the larger gyroradii for larger particles as shown in Figure 11). The fast rotators therefore impose the minimum requirements on the mass transport to sustain the hot excesses. As a result, they should be most likely to show hot excesses.

6. MASS TRANSPORT TO THE INNER REGIONS AND THE COLLISIONAL TIMESCALE OF NANOGRAINS

The viability of our model depends on the total mass that is transported into and maintained at the inner regions near the sublimation radius. The relation between various timescales in the system determines the amount of dust continuously present in the inner regions. Below we give analytic estimates of the mass transport and collisional timescales of the nanograins, and the steady-state levels of dust.

6.1. Mass transport into the inner regions and nanograin production rate

To estimate the total amount of dust that can be theoretically transported into the inner regions of early-type star disks from outer asteroid-belt analog dust rings via PRD, we use the derivation in van Lieshout et al. (2014), their Equation (11) (which assumes a single grain size). This yields 2×10^{14} kg yr⁻¹ for our reference model from an outer region at 10 AU.

6.2. Collisional timescale for nanograins

There are two significant loss mechanisms for nanograins in this situation: sublimation or sputtering, and grain-grain collisions. Sputtering will be modest around A-type stars given their small winds, but will be dominant around later types (Wurz 2012). Sublimation is not well understood because the grain properties may differ from those of bulk material of the same composition, and the composition of the nanograins is not well determined. We treated sublimation as in Kobayashi et al. (2011), derived for larger grains.

The dynamical models presented in Section 4.5 show that the nanograins produced via sublimation are able to remain in the system for a considerable amount of time. The largest nanograins de-orbit into the central star within a few decades. Since their production rate can be of order 10^{14} kg yr⁻¹, compared with our rough estimate of a mass of 10^{15} kg needed to produce a typical hot excess (Section 3.1), magnetic field trapping is a viable model to explain this phenomenon if the nanograins are not destroyed via other mechanisms. The dominant loss mechanism for the nanograins is collisions, which we must quantify to understand the equilibrium grain density.

The effects of collisions have been studied numerically by Ohnishi et al. (2008). They modeled collisions of grains of radii 1.4 and 4 nm with relative velocities of 3.6 - 6.1 km s⁻¹, and at temperatures appropriate for the interstellar medium. They found a variety of outcomes such as grain fusion, melting and nucleation. In general, grazing collisions did not destroy the grains, although as expected, direct ones did. A limited study of hydrocarbon nanograin collisions at higher velocities (Papoular 2004) reached qualitatively similar conclusions. The mutual cross section for the collision of two identical grains is $4\pi s^2$; however, to allow for survival of a significant fraction of a grain in a grazing collision, in the following we will assume that the cross section for grain destruction is the projected area of a single grain, πs^2 .

The collisional timescale of a particle in a particle-in-a-box system with particles of the same size is the inverse of its collisional probability, i.e.

$$t_{\text{coll}}(s) = P_{\text{coll}}(s)^{-1} = [n(s)v(s)\pi s^2]^{-1}, \quad (19)$$

where $n(s)$ is the number density of the particles. Assuming a single particle size, we analytically determine an estimate for the collisional timescale of a particle as a function of its size. The flux emitted by a single nanograin will be

$$f(\nu; s)[\text{Jy}] = 10^{26} \frac{\pi \lambda^2}{D^2 c} s^2 Q_{\text{abs}}(s) B_{\text{RJ}}. \quad (20)$$

where Q_{abs} is the absorption (emission) efficiency of the grain, B_{RJ} is the Rayleigh-Jeans approximation to a blackbody, and D is the distance from Earth. As an example, a fit to the Q_{abs} curves of carbon nanograins in size up to ~ 100 nm and for wavelengths of 1 - 10 μm yields

$$Q_{\text{abs}}(\lambda = 1 - 10 \mu\text{m}) \approx 3 \left(\frac{s}{\mu\text{m}} \right) \left(\frac{\lambda}{\mu\text{m}} \right)^{-1.5}. \quad (21)$$

Therefore, the near-IR emission from a single nanograin can be written as

$$f(\nu; s)[\text{Jy}] = 6 \times 10^{23} \frac{\pi k_{\text{b}} T}{D^2} \frac{s^3}{\lambda^{3.5}}. \quad (22)$$

We assume the nanograins to be super-heated to 2000 K once they are created. The number density can be expressed as

$$n(s) = \frac{F(\nu)}{f(\nu; s)V(s)}, \quad (23)$$

where $F(\nu)$ is the total amount of excess emission. The collisional volume is calculated as

$$V(s) = \frac{\pi h}{2} \left[r_{\text{sub}}^2 - (r_{\text{sub}} - r_{\text{gyro}})^2 \right] [r_{\text{sub}} + (r_{\text{sub}} - r_{\text{gyro}})], \quad (24)$$

where h is the disk aspect ratio, which we take to be 0.2. In the left panel of Figure 13, we plot the collisional timescales of single particles calculated using this simple analytic assumption as a function of assumed single grain sizes for some of the well known systems with hot excess. We plot the assumed system parameters in Table 3. The gyroradii of the particles and their collisional velocities (orbital velocity reduced) were calculated with our numerical model. The largest nanograins have the longest survival timescales, of order a few months to even a few years in each system.

6.3. Required mass transport rate

Here, we investigate the total mass transport necessary to yield detectable levels of 2 micron excess emission. For this, we need to calculate the equilibrium particle density resulting from a continuous mass transport and collisional destruction. Since the magnetic field trapping timescale (i.e., in the absence of collisions) is many orders of magnitude longer than the collisional destruction timescale, we do not include it in the following calculation.

The rate at which characteristic sized particles are transported into the inner regions will be

$$\tau_{\text{prd}} = \frac{\dot{M}}{m(s)}, \quad (25)$$

while the collisional rate is expressed by

$$\tau_{\text{coll}} = \frac{N(s)^2}{V(s)^2} v(s) \pi s^2 V(s). \quad (26)$$

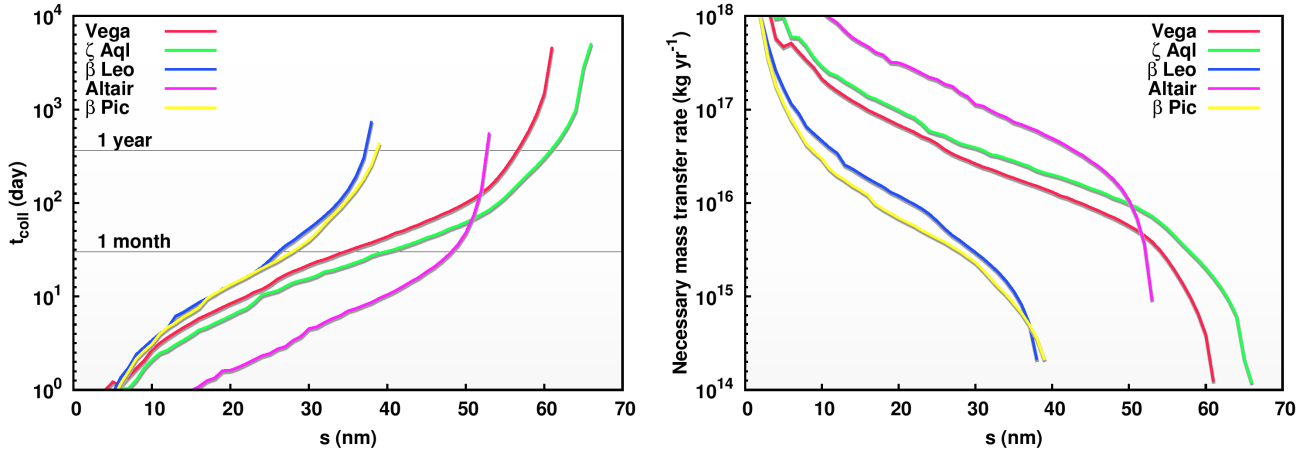


Figure 13. The collisional timescale for some well known hot-excess systems assuming a single characteristic nanograin size and the necessary mass transfer rate to allow a steady-state hot emission.

Table 3
Adopted stellar properties for mass transport calculations

Star	M_* (M_\odot)	R_* (R_\odot)	L_* (L_\odot)	r_{sub} (AU)	T_{rot} (h)	D (pc)	F (Jy)	S_{max} (nm)
Vega	2.13	2.36	40	0.30	12.5	7.67	8.17	60
ζ Aql	2.37	2.27	40	0.30	8.7	25.45	0.79	64
β Leo	1.78	1.73	15	0.18	16.3	11.00	1.09	38
Altair	1.79	1.80	11	0.16	8.9	5.12	16.48	53
β Pic	1.75	1.80	9	0.15	16.8	19.44	0.21	40

where $N(s)$ is the total number of particles of radius s . Using the flux estimates of single size particles in Equation (22) and the collisional volume and velocity determined by the numerical models, the necessary mass transport rate to yield a detectable level of steady-state particles is

$$\dot{M} = \left[\frac{F(\nu, s)}{f(\nu, s)} \right]^2 \frac{4v(s)\pi^2 s^5 \rho}{3V(s)}. \quad (27)$$

We plot the mass transfer estimates using single particle sizes in Figure 13 for the systems listed in Table 3. The required mass transfer for the systems is in agreement with the analytic estimates we calculated in the previous section, i.e., under our assumptions the expected mass transport is adequate to account for required amount of hot dust.

7. ASTEROIDS AND COMETS

As is often the case for detectable debris disk components (Wyatt 2005), PRD may work too slowly to bring adequate material inward to account for the brightest cases of hot dust emission. A more rapid, although less well constrained, transport process is through asteroids and comets that are deflected into orbits that bring them close to the star - for brevity, we will refer to both as “comets.” The above discussion illustrates the physics involved in grain creation, trapping, and survival for this case also. As such objects disintegrate, they leave trails of grains and larger fragments along their Keplerian orbits. There can be a significant population of nanograins in comet ejecta possibly originally from the interstellar medium (e.g., McDonnell et al.

1987; Greenberg & Hage 1990), and more nanograins will be produced as the larger particles are eroded by sublimation. As soon as the nanograins are exposed to the radiation of our reference A-star, they will become strongly charged electrically and will be deflected from the Keplerian orbits of the comet and will orbit with the magnetic field. Therefore, they will be trapped in orbits similar to those discussed in the previous section. This process will be expedited because many of the “larger” grains are likely to be very poorly consolidated clusters of nanograins (e.g., Greenberg & Hage 1990; Dominik et al. 2007; Sanders & Velbel 2012) that will fall apart in the harsh environment close to the star. However, an important distinction compared with the discussion in the previous section is that their orbits can originate from a much broader range of distances from the star, i.e., from any distance to which a larger body has survived. Therefore, there will be a lower space density for a given mass of nanograins, and the destruction rate by collisions will be lower.

To evaluate the requirements for this transport mechanism, we assume that the nanograins have a typical lifetime of four months, that the comet producing them has a density of 1 g cm^{-3} , that 7% of the comet mass is already (McDonnell et al. 1987; Sanders & Velbel 2012) or is converted to nanograins, and that an equilibrium mass of 10^{15} kg of nanograins is required to produce the hot excess (Section 3.1). The destruction of three comets a year, each of 15 km radius, is then sufficient to produce a hot excess of $\sim 1\%$ at $2 \mu\text{m}$ around our reference A-star. Thus, plausible additional mass transport in this manner can augment that from PRD and make the models for the hot dust more robust.

8. TESTABLE PREDICTIONS OF THE MODEL

There are three results of our modeling that can be tested: 1.) in Section 3.1 we derived some general requirements imposed by the observed roughly Rayleigh-Jeans spectrum of the hot excesses; 2.) in Section 5.3, we found that rapidly rotating stars should be able to retain larger equilibrium populations of nanograins than slow rotators; and 3.) in Section 5.2 we pointed out that very large magnetic fields would result in rapid nanograin destruction and that one should therefore not necessarily

expect stars with such fields to have large excesses. In this third case, since the type of A-star with large magnetic fields also rotates slowly, we can only test the effect of the two variables together. We examine each of these predictions in turn.

8.1. *Spectrum and size of emitting regions*

We deduced in a general way in Section 3.1 that the emitting grains could not be larger than about 200 nm, to avoid producing too much radiation at 10 μm . In Section 4.4 we derived an upper limit of 121 nm for the size of grains that could be trapped magnetically around our reference A-star. It is inherent in the general behavior of the hot excesses that the grains must be close to the star, and this has been confirmed directly for Vega (Menneson et al. 2011). By trapping nanograins as they are released near 0.2 AU due to sublimation or breakdown of comets, this requirement is automatically satisfied by our hypothesis for the hot excesses.

8.2. *Rotation rates and hot excesses*

We now consider the prediction of an association of hot excesses with rapidly rotating stars. To compare rotation rates, we used $v\sin i$ ¹⁰. Although rotation determination from this parameter is uncertain for any individual star due to unknown inclination effects, a large value is an unequivocal indication of fast rotation, allowing us to compare stars known to rotate rapidly with a mixed control sample. We confined the sample to spectral types of F2V and earlier (and excluded giants), since spin down is a dominant issue otherwise. We found that the average $v\sin i$ for stars in Absil et al. (2013) and Ertel et al. (2014) without detected hot excesses is 141 ± 20 km s⁻¹, where we quote the error of the mean based on the rms scatter of the measured values for stars without hot excesses. Similarly, $v\sin i$ for the stars with detected excesses is 210 ± 27 km s⁻¹, with the error quoted for the mean and based on the rms scatter of the measured values for the stars with hot excesses¹¹. The difference is 69 ± 34 km s⁻¹, that is at 2σ significance, or with a 2.3% probability of being due to chance (given that the difference is in the predicted direction). We did not include Vega in any of these averages because it has a small $v\sin i$ but is known to be a very rapid rotator. However, it adds to the evidence that hot excesses are associated with rapid rotation. Therefore, the prediction that hot excesses would tend to be found in rapidly rotating stars is supported.

8.3. *Excesses in Ap/Bp stars*

Naively, if a little magnetic field is good for hot excesses, one might expect that a lot of magnetic field would be better. However, our modeling indicates that this expectation may not be fulfilled: stars with strong magnetic fields will confine nanograins more tightly, resulting in a higher rate of collisions and more rapid

nanograin destruction. We used a sample of Ap stars to test this possibility. Many of the chemically peculiar Ap stars have measured fields of tens to hundreds of Gauss, and it is believed that such fields are a general characteristic of the class (e.g., Aurière et al. 2007; Mathys 2009; Braithwaite 2014; Kochukhov 2014). However, these stars are also slow rotators (Tassoul 2004), so they provide a mixed test for the effects of magnetic fields and of rotation.

To look for excesses around Ap stars, we started with the McDonald et al. (2012) list of stars. We accepted only those members with modeled temperatures between 6500 K and 13,000 K. We drew an initial sample of Ap and Bp star candidates on this list from Renson & Manfroid (2009). We flagged all likely Ap, Am, or HgMn stars and then used the information in Skiff (2014) to eliminate all but the Ap and Bp ones. There are ~ 460 Ap and Bp stars in the McDonald et al. (2012) study with usable 2MASS photometry. For a control sample, we accepted all 19473 non-Ap stars in McDonald et al. (2012) meeting our input criteria. We found no evidence for hot excesses in the $J - K_S$ colors between the Ap stars and the control sample. The large magnetic fields in Ap/Bp stars do not appear to result in a high incidence of hot excesses. This result may arise because the effect of slow rotation in these stars overcomes any trend toward magnetic nanograin trapping.

In fact, the average $J - K_S$ color of the Ap stars relative to the trend for normal A stars is slightly (-0.008 mag) negative, which may be a result of subtle spectral differences due to their anomalous abundances. Another possibility is their slow rotation (Tassoul 2004) and the resulting relatively uniform surface temperatures. That is, rapid rotation will establish a temperature gradient over the surface of the star, with the equatorial region cooler than the polar ones because of its larger radius. Spectral typing is done in the optical, where the hot polar regions will be relatively prominent. For A-stars, the $J - K_S$ color is largely in the Rayleigh-Jeans regime, where the contribution of the cooler equatorial regions will be relatively greater than in the optical. Thus, a sample of stars that includes many rapidly rotating ones might have a $J - K_S$ colors redder than implied by the spectral types, whereas a sample of slowly rotating stars should have $J - K_S$ matching the spectral types more closely.

8.4. *Rotation and infrared colors*

The possibility that rapid rotating stars might show anomalously red infrared colors for their spectral types would undermine the argument of slightly red $J - K$ for hot excess stars that we made in Section 2 and for slow rotation contributing to the lack of such an excess for Ap/Bp stars just above. Vega can be taken as an extreme example, since it is rotating nearly at the breakup rate and is virtually perfectly pole-on, maximizing the exposure to the hot poles and resulting in the assignment of a relatively early spectral type (Aufdenberg et al. 2006; Castañeda et al. 2014). Rieke et al. (2008) estimate that as a result $J - K_S$ is 0.01 mag redder than expected for the assigned spectral type; given the extreme nature of Vega, an effect of 1 – 2% is an upper limit to what might occur with other stars.

We used the McDonald et al. (2012) sample to test

¹⁰ $v\sin i$'s for HIP 21589, 27288, 27321, 41307, 53910, 54872, 57632, 59774, 60965, 61622, 87108, 88771, 93747, 94114, 97649, 98495, & 105199 are from Zorec & Royer (2012), for HIP 50191 & 71908 from Glebocki & Gnacinski (2005), for HIP 2072, 11001, 102333, & 109285 from van Belle (2012), for HIP 71284 from Royer et al. (2002), and for HIP 74824 from Diaz et al. (2011).

¹¹ $v\sin i \sim 200$ km s⁻¹ corresponds to a rotational period of ~ 10 hours for a star viewed from the equatorial direction.

for this effect. We took all members of the sample with $v_{\text{ini}} \geq 200 \text{ km s}^{-1}$ and compared their $J - K_S$ with the sample members with smaller v_{ini} , taking rotation measures from Glebocki & Gnacinski (2005); Zorec & Royer (2012). The comparison is made difficult by the relatively large number of 1.) rapidly rotating emission-line stars, which need to be excluded because of the potential of K-band excesses due to free-free emission, 2.) stars with faint red companions, which were reduced by eliminating those detected in the X-ray (De Rosa et al. 2011), and 3.) binaries in general. The latter category is troublesome because tidal locking in close binaries can sustain fast rotation and hence bias the sample due to undetected close companions. To eliminate such cases, we rejected all examples with $J - K_S \geq 0.08$, on the basis that this value is substantially larger than the 1–2% possible solely from fast rotation and indicates an excess due to another cause. We also rejected the few cases with $J - K_S \leq -0.08$.

The average $J - K_S$ for the stars with the higher v_{ini} was larger by $0.003 \pm 0.002 \text{ mag}$. In Section 8.2 we found indications that hot excesses tend to be associated with large v_{ini} . According to Absil et al. (2013), about 50% of A-stars have hot excesses at typical levels of $\sim 1\%$. Therefore, the apparent tiny excess at K_S could just arise from the expected number and extent of hot dust excesses. There is no convincing effect of rapid rotation on the intrinsic stellar $J - K_S$ color. We therefore believe that the result in Section 2 is valid and that the small color difference for the Ap stars is primarily due to a spectral effect arising from their anomalous abundances.

9. CONCLUSIONS

We have studied the hot near-infrared excesses detected by interferometric measurements, particularly of A-stars. Our main conclusions are:

1. Infrared photometry shows a slightly (1.1%) redder $J - K_S$ color for stars reported to have these excesses than for those reported not to have excesses. Although only at $\sim 1.5 \sigma$ significance, this result supports the reality of the detections.
2. Given the roughly Rayleigh-Jeans spectral energy distributions of the excesses, we conclude in agreement with previous studies that they must be generated by hot dust grains less than 200 nm in radius. Under typical assumptions for circumstellar dusty debris, such grains would be blown away from A-stars by radiation pressure force.
3. However, the grains will rapidly acquire significant electrical charge. We demonstrate that these charged grains can have significant trapping times in the stellar magnetic field via Lorentz forces that place the particles on epicyclic orbits. Trapping occurs even for fields as small as 0.1 G, less than the field strengths measured for Sirius and Vega.
4. Magnetic trapping also naturally accounts for other aspects of the hot grain population; it imposes an upper limit on the grain sizes of just over $\sim 100 \text{ nm}$, it keeps the grains at 0.1 - 0.2 AU from the star, and it can maintain a sufficient steady-state population of grains to account for the hot emission.

5. Additional predictions from the trapping model, that the hot excesses are likely to be associated with rapid stellar rotation and that such excesses would not be preferentially associated with very large magnetic fields, are also supported by observation.

10. ACKNOWLEDGEMENTS

We thank Kaitlin Kratter, Mike Sitko, Rik van Lieshout, Mark Wyatt and the anonymous referee for helpful comments. This work was supported by NASA grants NNX13AD82G and 1255094. This publication makes use of data products from the Two Micron All Sky Survey, which is a joint project of the University of Massachusetts and the Infrared Processing and Analysis Center/California Institute of Technology, funded by the National Aeronautics and Space Administration and the National Science Foundation. This research also has made use of the VizieR catalogue access tool, CDS, Strasbourg, France. The original description of the VizieR service was published in A&AS 143, 23.

REFERENCES

- Absil, O., di Folco, E., Mérand, A. et al. 2006, A&A, 452, 237
 Absil, O., di Folco, E., Mérand, A. et al. 2008, A&A, 487, 1041
 Absil, O., Defrère, D., Coudé du Foresto, V., Di Folco, E. et al. 2013, A&A, 555, 104
 Akeson, R. L., Ciardi, D. R., Millan-Gabet, R. et al. 2009, ApJ, 691, 1896
 Alina, D., Petit, P., Lignières, F., et al. 2012, AIPC, 1429, 82
 Allen, D. A. & Cragg, T. A. 1983, MNRAS, 203, 777
 Aufdenberg, J. P., Mérand, A., Coudé du Foresto, V. et al. 2006, ApJ, 645, 664
 Aumann, H. H., & Probst, R. G. 1991, ApJ, 368, 264
 Aurière, M., Wade, G. A., Silvester, J., Lignières, F. et al. 2007, A&A, 475, 1053
 Babel, J. 1995, A&A, 301, 823
 Bonsor, A., Raymond, S. N., & Augereau, J.-C. 2013, MNRAS, 433, 2938
 Bonsor, A., Raymond, S. N., Augereau, J.-C., & Ormel, C. W. 2014, MNRAS, 441, 2380
 Bouchet, P., Schmider, F. X., & Manfroid, J. 1991, A&AS, 91, 409
 Braithwaite, J., & Cantiello, M. 2013, MNRAS, 428, 2789
 Braithwaite, J. 2014, Proc. IAU Symp., 302, 255
 Burns, J. A., Lamy, P. L., & Soter, S. 1979, Icarus, 40, 1
 Carpenter, J. M. 2003, <http://www.astro.caltech.edu/~jmc/2mass/v3/transformations/>
 Carter, B. S. 1990, MNRAS, 242, 1
 Casagrande, L., Ramirez, I., Meléndez, J., Bessell, M., & Asplund, M. 2010, A&A, 512, 54
 Castañeda, D., Deupree, R. G., & Aufdenberg, J. P. 2014, *astroph* 1411.1673
 De Rosa, R. J. Bulger, J., Patience, J. et al. 2011 MNRAS, 415, 854
 Diaz, C. G., Gonzalez, J. F., Levato, H., & Grosso, M. 2011, A&A, 531, 143
 Defrère, D., Absil, O., Augereau, J.-C. et al. 2011, A&A, 534, 5
 De Rosa, R. J., Bulger, J., Patience, J. et al. 2011, MNRAS, 415, 845
 Dominik, C., Blum, J., Cuzzi, J. N., & Wurm, G. 2007, *Protostars & Planets*, page 783.
 Ertel, S., Absil, O., Defrère, D. et al. 2014, A&A, 570, 128
 Fedkin, A. V., Grossman L., & Ghiorso, M. S. 2007, *Geochimica et Cosmochimica Acta*, 70, 206
 Glass, I. S. 1974, MNSSA, 33, 53
 Glebocki, R. & Gnacinski, P. 2005, ESA SP-5600, 571
 Greenberg, J. M., & Hage, J. I. 1990, ApJ, 361, 260
 Ignatov, A. M. 2009, *Plasma Physics Reports*, 35, 647
 Johnson, H. L., Mitchell, R. I., Iriarte, B., & Wisniewski, W. Z. 1966, *Comm. Lun. Plan. Lab.*, 4, 99

- Kazenas, E. K., & Tsvetkov, Yu. V. 2008, "Thermodynamics of the Evaporation of Oxides"
- Kidger, M. R. & Martín-Luis, F. 2003, *AJ*, 125, 3311
- Kimeswenger, S., Lederle, C., Richichi, A. et al. 2004, *A&A*, 413, 1037
- Kobayashi, H., Watanabe, S.-I., Kimura, H., & Yamamoto, T. 2009, *Icarus*, 201, 395
- Kobayashi, H., Kimura, H., Watanabe, S.-I., Yamamoto, T., & Müller, S. 2011, *Earth, Plan., & Spc*, 63, 1067
- Kochukhov, O. 2014, "Putting A Stars into Context: Evolution, Environment, and Related Stars," Publishing House "Pero", pp. 389-397
- Koen, C., Marang, F., Kilkenny, D., & Jacobs, C. 2007, *MNRAS*, 380, 1433
- Lamoreaux, R. H., Hildenbrand, D. L., & Brewer, L. 1987, *J. Phys. Chem. Ref. Data*, 16, No. 3
- Lebreton, J., van Lieshout, R., Augereau, J.-C. et al. 2013, *A&A*, 555, 146
- Lefevre, J. 1975, *A&A*, 41, 437
- Lignières, F., Petit, P., Böhm, T., & Aurière, M. 2009, *A&A*, 500, 41
- Liou, J.-C., & Zook, H A. 1999, *AJ*, 118, 580
- Ma, Q., Matthews, L. S., Land, V., & Hyde, T. W. 2013, *ApJ*, 763, 77
- Mann, I., Köhler, M., Kimura, H., Czechowski, A., & Minato, T. 2006, *Astron. Astrophys. Rev.*, 13, 159
- Mann, I., Murad, E., & Czechowski, A. 2007, *Plan. & Space Sci.*, 55, 1000
- Mann, I., Meyer-Vernet, N., & Czechowski, A. 2014, *Physics Reports*, 536, 1
- Mathys, G. 2009, *ASP Conf. Ser.* 405, 473
- Mawet, D., Mennesson, B., Serabyn, E., Stapelfeldt, K., & Absil, O. 2011, *ApJL*, 738, 12
- McDonald, I., Zijlstra, A. A., & Boyer, M. L. 2012, *MNRAS*, 427, 343
- McDonnell, J. A M., Alexander, W. M., Burton, W. M. et al. 1987, *A&A*, 187, 719
- McGregor, P. J. 1994, *PASP*, 106, 508
- Mennesson, B., Serabyn, E., Hanot, C, Martin, S. R., Liewer, K., & Mawet, D. 2011, *ApJ*, 736, 14
- Mennesson, B., Milan-Gabet, R., Serabyn, E., Colavita, M. M. et al. 2014, *ApJ*, 797, 119
- Ohnishi, N., Bringa, E. M., Remington, B. A., et al. 2008, *J. Phys. Conf. Series*, 112, 042017
- Palik, E. D. 1997, "Handbook of Optical Constants of Solids," Academic Press: Waltham, MA, USA
- Papoular, R. 2004, *A&A*, 414, 573
- Parker, E. N. 1958, *ApJ*, 128, 664
- Parker, E. N. 1964, *ApJ*, 139, 951
- Pedersen, A., & Gómez de Castro, A. I. 2011, *ApJ*, 740, 77
- Petit, P., Lignières, F., Aurière, M., Wade, G. A. et al. 2011, *A&A*, 532L, 13
- Pickles, A., & Depagne, É. 2010, *PASP*, 122, 1437
- Raymond, S. N. & Bonsor, A. 2014, *MNRAS*, 442L, 18
- Renson, P., & Manfroid, J. 2009, *A&A*, 498, 961
- Rieke, G. H., Blaylock, M., Decin, L. et al. 2008, *AJ*, 135, 2245
- Royer, F., Grenier, S., Baylac, M.-O., Gómez, A. E., & Zorec, J. 2002, *A&A*, 393, 897
- Sanders, N. E., & Velbel, M. A. 2012, *Meteoritics & Plan. Sci.*, 47, 594
- Schatten, K. H., Wilcox, J. M., & Ness, N. F. 1969, *Solar Phys.*, 6, 442
- Skiff, B A. 2014, *VizieR Online Data Catalog of Stellar Spectral Types*
- Su, K. Y. L., & Rieke, G. H. 2014, *IAU Symp.*, 299, 318
- Tassoul, J.-L. 2004, "Stellar Rotation," Cambridge University Press: Cambridge, UK, page 192
- UKIRT bright standards available at <http://www.gemini.edu/sciops/instruments/near-ir-resources/nir-photometric-standard-stars/ukirt-bright-standards>
- van Belle, G. T. 2012, *Ast. & Astrophys. Rev.*, 20, 51
- van Lieshout, R., Dominik, C., Kama, M., & Min, M. 2014, *A&A*, 571, 51
- Voges, W., Aschenbach, B., Boller, Th. et al. 1999, *A&A*, 349, 389
- Weingartner, J., & Draine, B. 2001, *ApJS*, 134, 263
- Wolf, S. 2015, <http://www1.astrophysik.uni-kiel.de/dds/>
- Wurz, P. 2012, in "Nanodust in the Solar System: Discoveries and Interpretations," ed. I Mann, N. Meyer-Vernet, A. Czechowski, Springer: Heidelberg, pp 161-178
- Wyatt, M. C., 2005, *A&A*, 433, 1007
- Wyatt, M. C. 2008, *ARA&A*, 46, 339
- Zorec, J., & Royer, F. 2012, *A&A*, 537, 120

APPENDIX

Procedures to transform heritage photometry to 2MASS

We have assembled as much high-quality J, H, K_S photometry as possible for bright stars. We evaluated various sources of heritage near-infrared photometry and accepted those that appeared to have good internal accuracy and that could be transformed accurately onto the 2MASS system. For this paper, we took photometry from:

1. 2MASS for HD 15008, 134083 & 210049;
2. Allen & Cragg (1983) for HD 15798 & 71155;
3. Aumann & Probst (1991) (which we found to be consistent with the CIT system) for HD 2262*, 15008, 30652, 38678, 39060*, 102647*, 104731*, 106591, 128167, 134083, 135379, 139664, 142860, 164259, & 210302*;
4. Carter (1990) for HD 2262*, 15798, 39060*, 71155, 88955, 97603, 108767*, 109787, 129502, & 210049;
5. the ESO standards list (Bouchet et al. 1991) for HD 2262*, 15008, 39060*, 71155, 88955, 109787, 135379, 178253, 197692, & 210049;
6. Glass (1974) for HD 15798, 39060*, 71155, 97603, 108767*, 109787, 129502;
7. Johnson et al. (1966) (where we accepted only stars measured at least three times under good conditions) for HD 22484, 30652, 48737, 88955, 95418, 97603, 102647*, 104731*, 106591, 108767*, 128167, 129502, 134083, 142860, 161868, 177724*, 187642*, & 203280*;
8. Kidger & Martín-Luis (2003) for HD 29388 & 187642*;
9. Kimeswenger et al. (2004) for HD 102647*;
10. McGregor (1994) for HD 15798, 71155;

11. Su, K. Y. L. & Rieke, G. H. (unpublished) for HD 3302, 22001, 135379, 160032, 188228, 197157, 197692, 210302*, & 213845 (SAAO system);
12. and the UKIRT standards list for HD 102647* & 128167.

The stars with hot excesses are indicated by * and can be seen to be distributed similarly to the other stars, e.g., their photometry should be homogeneous with that for stars without hot excesses.

We used transformations from Carpenter (2003) to convert photometry from the Anglo-Australian Observatory, CIT, ESO, and UKIRT systems to the 2MASS one. To convert SAAO to 2MASS we used Koen et al. (2007). We also derived transformations as follows:

- $K(2MASS) = K(\text{Johnson}) - 0.0567 + 0.056(J-K)$
- $J(2MASS) = J(\text{Johnson}) - 0.69 + 0.0285(J-K)$
- $K(2MASS) = K(\text{Kidger}) + 0.008 + 0.0257(J-K)$
- $J(2MASS) = J(\text{Kidger}) - 0.0199 + 0.0483(J-K)$
- $K(2MASS) = K(\text{Kimeswenger}) - 0.006$
- $J(2MASS) = J(\text{Kimeswenger})$

It is difficult to estimate errors for transformed photometry. A number of tests indicated that the products have similar errors as the 2MASS photometry and track the 2MASS colors well. Therefore, where there were multiple measurements of a star, we averaged them with equal weights after transforming them onto the 2MASS system.